

Numerical and Experimental Investigations of the Oscillatory Flow Inside Standing Wave Thermoacoustic System at Two Different Flow Frequencies


 Open
Access

 Fatimah Al Zahrah Mohd Saat^{1,2,*}, Siti Hajar Adni Mustaffa¹, Fadhilah Shikh Anuar^{1,2}
¹ Fakulti Kejuruteraan Mekanikal, Universiti Teknikal Malaysia Melaka, Hang Tuah Jaya, 76100, Durian Tunggal, Melaka, Malaysia

² Centre for Advanced Research on Energy, Universiti Teknikal Malaysia Melaka, Hang Tuah Jaya, 76100, Durian Tunggal Melaka, Malaysia

ARTICLE INFO

Article history:

Received 16 July 2019

Received in revised form 7 August 2019

Accepted 21 August 2019

Available online 31 August 2019

ABSTRACT

Energy crisis has led to the search of sustainable and green technology and thermoacoustics have been recognised as one of them. One of the challenging issue with this emerging technology is the difficulty in understanding the complex fluid dynamics phenomena of the oscillatory flow of the acoustic wave inside the system. In this paper, computational fluid dynamics (CFD) models of a standing wave thermoacoustic flow conditions are solved using ANSYS Fluent and the CFD results are validated with experimental data from a similar setup; standing wave flow conditions with two resonance frequencies of 13.1 Hz and 23.1 Hz. Good match of velocity amplitude data was found between the CFD and the experimental results, particularly for the low flow frequency of 13.1 Hz. Similar trend of velocity results between numerical models and experimental results of higher frequency of 23.1 Hz is also observed. As frequency increases, the velocity amplitude did not change much but the displacement of fluid becomes smaller. This causes the vortex to travel rapidly but at a shorter distance into and out of the channel when the fluid flows at higher frequency of 23.1 Hz. The amplitude of annular flow also becomes closer to the wall because the viscous penetration depth becomes thinner as frequency increases. These results help in understanding the impact of frequency variations on fluid dynamics aspect of the standing wave inside the emerging technology of thermoacoustic systems.

Keywords:

Oscillatory flow; CFD; thermoacoustics; standing wave

Copyright © 2019 PENERBIT AKADEMIABARU - All rights reserved

1. Introduction

Energy crisis and environmental issues have led to the search for efficient and sustainable technologies that fulfil the human needs and at the same time minimizing the bad impact on the earth [1]. This includes efforts to improve the current system with innovative working fluids such as nanorefrigerants [2] or ventures into emerging and sustainable technologies such as thermoacoustics [3, 4]. The fluid inside thermoacoustic systems is flowing in an oscillatory condition [3, 4]. In oscillatory flow, fluid flows back and forth in a cyclic manner. It is this feature of the flow, alongside other conditions, that helps thermodynamic cycle to be achieved so that power production or

* Corresponding author.

E-mail address: fatimah@utem.edu.my (Fatimah Al Zahrah Mohd Saat)

cooling/heat pumping effects can be produced when acoustic wave comes into contact with solid surfaces [5]. This leads to an energy system that is based on thermoacoustic principles. The basic thermoacoustic energy system, which operates with standing wave condition, consists of an acoustic driver, heat exchangers, resonator and structures known as 'stack' or 'regenerator' [5, 6]. Additional features such as valves, loop tubes and buffer tubes are sometimes present especially when special features are needed for the system [5, 7]. Many prototypes of power production devices/engines [4,5,8-12] and refrigerators [5, 6, 13-16] using the thermoacoustic principle have been built to date. Even a system that coupled the thermoacoustic engine with thermoacoustic refrigerator have also been demonstrated [7, 15, 17]. These thermoacoustic systems offer attractive alternatives to the conventional systems as the system works with noble gaseous that are harmless to environment. In addition, the system uses very minimum moving parts and hence reduces the worries related to maintenance. These qualities made the thermoacoustic technology as one of the promising sustainable and green technologies.

Unfortunately, the complex nature of heat transfer as well as fluid dynamics of the flow inside thermoacoustic environment is less known leading to difficulties to accurately predict the system performance [5]. Many investigations argued on the validity of linear theoretical equations especially in the presence of nonlinearity of flow (i.e. streaming, temperature driven flow, turbulence, etc.) [3, 4, 18]. Therefore, more studies are needed for a better prediction of the flow behavior and heat transfer for this promising technology. As the heat is related to fluid dynamics, its flow behavior must also be studied and well understood. However, in order to emphasis on fluid dynamics of flow the heat component could be put aside first so that the study can be made to focus on the fluid dynamics part without too many interferences [19]. In this investigation, the fluid dynamics models are solved for two different flow frequencies and an experimental work has been conducted to validate the models. The models and experimental setup reported in this paper will help in the future investigation on the details of the fundamental aspects of fluid dynamics and heat transfer in the flow environment that is related to thermoacoustic systems.

2. Methodology

In this section, the methodology of the study is presented. The section starts with general description about the standing wave thermoacoustic system and then followed by the explanation of the numerical models. For a less known oscillatory flow of thermoacoustics, validation of numerical model is important to help understand the real feature of the fluid dynamics of the flow. Hence, description of the experimental setup that was built for validation purposes is given at the end of this section.

2.1 Standing Wave Thermoacoustic System with Quarter Wavelength Dimension

The investigation involves a standing wave thermoacoustic system with a quarter wavelength dimension. The system is as shown in Figure 1. The system consists of a loudspeaker as an acoustic driver, a parallel-plate structure called "stack" and a resonance duct known as a "resonator". The study involves two flow frequencies, f of 13.1 Hz and 23.1 Hz. These frequencies led to two viscous penetration depth, δ_v , which are corresponding to 0.67 mm and 0.5 mm, respectively.

The height of the resonator, H , is 152.40 mm. In thermoacoustics, the resonator is commonly designed to work at resonance frequency so that optimum performance could be achieved. Hence, the length of the resonator, L , in this study depends on the resonance frequency that needs to be achieved in the quarter wavelength thermoacoustic system. For flow frequency of 13.1 Hz, the overall

length of the resonator is 6.6 m. While, for flow frequency of 23.1 Hz, the overall length of the resonator is shorter, $L = 3.8$ m. The stack is installed at a fixed location of $x_s = 0.17\lambda$ in the resonator. This corresponds to locations of 4.5 m and 2.6 m from the hard end of the resonator for flow frequencies of 13.1 Hz and 23.1 Hz, respectively. This position is chosen based on thermoacoustic effect as reported in Mohd Saat and Jaworski, [18]’s work. Note that the pressure antinode is a location where pressure amplitude of the acoustic wave is at a maximum value. In the current study, the pressure antinode is at the hard end of the resonator. This location is labelled as P_a in Figure 1.

Generally, the parallel-plates “stack” geometry was chosen because of its simplicity in both maintenance and fabrication. The parallel-plates configuration illustrates the “stack”, which consists of sixteen aluminium plates, with length, l of 200 mm and the thickness, d of 3 mm. In thermoacoustics, the ‘stack’ is an important solid structure where thermodynamic processes of the energy system take place [5]. In the current study, the plate is made of aluminium with thermal conductivity, k_t , of 237 W/m.K and specific heat capacity, c_p , of 903 J/kg.K. The size of the spacing between each plates, denoted as D , is 6 mm, as shown in Figure 1 (b). The arrangement of parallel-plates stack leads to the porosity of 66.76%. The porosity is defined as the ratio of the space of the stack that is occupied by air over the total space area. The formula, $\omega = 2\pi f$, is the angular frequency of the acoustic oscillation. The wave number is defined as, $k_a = 2\pi f/c$ (where c is a speed of sound = 346 m/s).

The loudspeaker generates an acoustic standing wave within the resonator. The acoustic coupling between the resonator and the loudspeaker generates a quarter-wavelength, $\lambda/4$, (defined as $\lambda = c/f$) acoustic wave. This quarter-wavelength resonator was chosen due to the lesser resonator wall losses compared to the longer ones [20]. The dashed-box in Figure 1 (a) represents the area of the computational domain to be discussed in the next subsection.

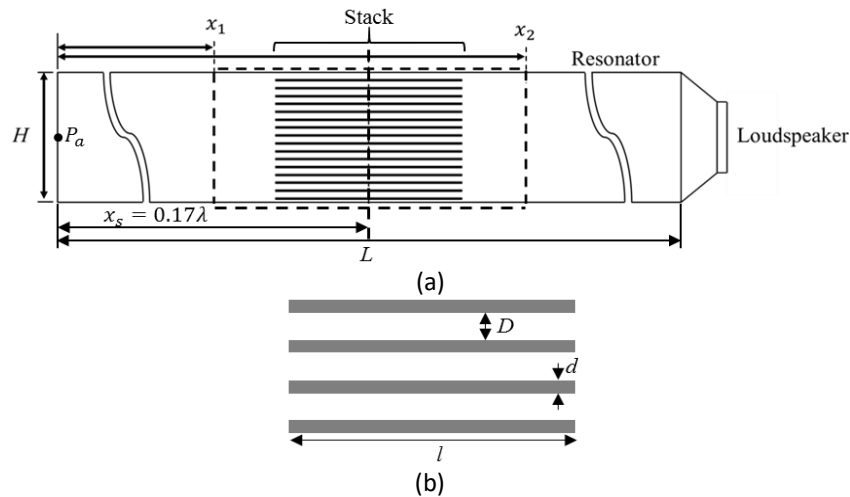


Fig. 1. Schematic diagram of (a) a quarter wavelength thermoacoustic system with a dashed box that represents the location of the computational domain and (b) the enlarged view of the ‘stack’ with only four plates shown

2.2 Numerical Models

The numerical model for a standing wave resonator was solved using ANSYS Fluent. Figure 2 presents the computational domain of a standing wave thermoacoustic system with parallel-plate structure known as ‘stack’ that is placed at the middle of the domain. The location of the computational domain is as shown in the dashed-box of Figure 1 (a). As also shown in Figure 1 (a),

the terms x_1 and x_2 which are corresponding to the inlet and outlet locations of the domain, respectively.

In the interest of reducing the computational time, a two-dimensional (2D) computational model was solved which focuses on the area around the “stack” - an important structure of any thermoacoustic system. The 2D model had been shown by earlier study to be sufficient to model the fluid dynamics of oscillatory flow inside thermoacoustic environment [18]. The 2D computational domain was built to cover a length of 300 mm on the left and right sides of the parallel-plates stack. The selection of the domain’s length is based on the suggestion by Feldmann and Wagner [21] where the length of the domain should not be made too short or too long.

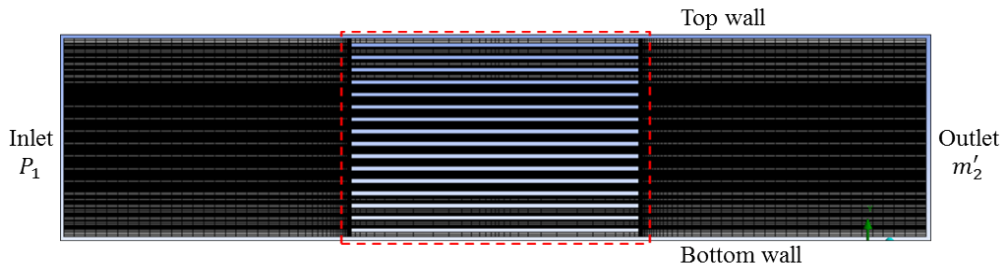


Fig. 2. The two-dimensional (2D) computational domain

The mesh was a quadrilateral type of mesh which was designed with a growth ratio of 1.2. The mesh was made denser within the channel of the parallel-plate structure and the areas nearby to capture the drastic change of the fluid dynamics of the flow within the areas. The mesh was tested for grid independency and it was found that the model with total grid number of 78780 is sufficient to provide results that are independence of the grid size. This corresponds to the y -plus value of 0.98. The smallest mesh was recorded with the size of 0.21 mm. The minimum orthogonality quality is 0.95 and the maximum skewness is 1.31×10^{-10} , which show that the mesh is in good quality conditions.

The models are solved for several flow amplitudes that are represented by a term known as a drive ratio, DR. The drive ratio is a ratio of the acoustic pressure at the location of pressure antinode, P_a , to the mean pressure, P_m . The mean pressure represents the atmospheric pressure inside the resonator. The working gas used is air (where mean pressure, $P_m = 10^5$ N/m² and mean air temperature, $T_m = 300$ K) and is modelled as an ideal gas. The thermal conductivity, k_t , is a function of temperature and it was modelled using a seventh-order polynomial equation, as expressed in Eq. (1). While, Eq. (2) presents the temperature-dependent mean dynamic viscosity, μ , which follows a power law model, and T_o is the reference temperature.

$$k_t = 0.023635 + 7.56264 \times 10^{-5}T - 2.5153710^{-8}T^2 + 4.18521 \times 10^{-12}T^3 + 1.05973 \times 10^{-15}T^4 - 1.12111 \times 10^{-18}T^5 - 5.47329 \times 10^{-22}T^6 - 9.94835 \times 10^{-26}T^7 \quad (1)$$

$$\mu = 1.85 \times 10^{-5} \left(\frac{T}{T_o} \right)^{0.76} \quad (2)$$

For each flow frequency, boundary conditions are set and applied at the boundaries; inlet, outlet, top and bottom walls of the domain (Figure 2). The oscillating pressure and oscillating mass flux, denoted as P_1 and m'_2 , were placed at the inlet and outlet locations of the domain, respectively. These inlet and outlet conditions are calculated using lossless equations as shown in Eq. (3) and (4),

$$P_1 = P_a \cos(k_a x_1) \cos(2\pi f t) \quad (3)$$

$$m'_2 = \frac{P_a}{c} \sin(k_a x_2) \cos(2\pi f t + \theta) \quad (4)$$

where the terms, P_a , k_a , f , t , θ , c , x_1 and x_2 represent acoustic pressure at the location of pressure antinode, wave number, flow frequency (Hz), time (s), phase (rad) and speed of sound (m/s), as well as locations of the inlet and outlet surfaces of the domain, respectively [18]. Tables 1 and 2 present the values of boundary conditions for models with flow frequencies of 13.1 Hz and 23.1 Hz, respectively.

Table 1

The boundary conditions for flow frequency of 13.1 Hz

Drive ratio, DR, (%)	Oscillating pressure, P_1 , (Pa)	Oscillating mass flux, m'_2 , (kg/s.m ²)	Reynolds number, Re, at the inlet, x_1	Turbulent intensity, TI , at the inlet, x_1	Reynolds number, Re, at the outlet, x_2	Turbulent intensity, TI , at the inlet, x_2
0.30	162.31	0.7885	235.43	0.0808	254.41	0.0800
0.45	243.46	1.1828	343.14	0.0768	383.52	0.0761
0.65	351.67	1.7084	508.53	0.0734	550.60	0.0727
0.83	449.05	2.1815	653.12	0.0712	706.28	0.0705
1.00	541.03	2.6284	786.03	0.0695	846.78	0.0689
1.20	649.24	3.1540	941.71	0.0680	1017.66	0.0673
1.50	811.54	3.9425	1177.14	0.0661	1272.07	0.0655
2.00	1082.06	5.2567	1568.25	0.0638	1697.36	0.0632
3.00	1623.09	7.8851	2354.28	0.0606	2544.14	0.0600

Table 2

The boundary conditions for flow frequency of 23.1 Hz

Drive ratio, DR, (%)	Oscillating pressure, P_1 , (Pa)	Oscillating mass flux, m'_2 , (kg/s.m ²)	Reynolds number, Re, at the inlet, x_1	Turbulent intensity, TI , at the inlet, x_1	Reynolds number, Re, at the outlet, x_2	Turbulent intensity, TI , at the inlet, x_2
0.30	170.87	0.8132	231.63	0.0810	262.01	0.0798
0.45	256.31	1.2198	345.55	0.0771	394.91	0.0758
0.65	370.22	1.7619	497.44	0.0736	569.58	0.0724
0.83	472.74	2.2499	637.93	0.0714	725.27	0.0702
1.00	569.57	2.7107	767.04	0.0697	873.36	0.0686
1.20	683.48	3.2528	918.93	0.0682	1051.83	0.0670
1.50	854.35	4.0660	1150.56	0.0663	1313.84	0.0652
2.00	1139.14	5.4213	1534.08	0.0640	1750.52	0.0629
3.00	1708.71	8.1320	2301.02	0.0608	2623.88	0.0598

For turbulence modelling, two additional boundary conditions are required to be set at the inlet and outlet surfaces of the domain; turbulent length scale, $\ell = 0.07D$, and turbulent intensity, $TI = 0.16(Re)^{-1/8}$. The Reynolds number, $Re = \rho U D / \mu$ (where ρ , U , D and μ represent density of the fluid, the first order harmonic of velocity amplitude of the flow, the size of the spacing between plates and dynamics viscosity, respectively). The velocity amplitude at inlet and outlet boundary conditions are calculated using theoretical formula where the mass flux as described in Eq. (4) was divided with density. Tables 1 and 2 show that the Reynolds number of the flow for all the models are relatively low. Hence, one may assume that laminar model may be sufficient to be used to represent the fluid dynamics of flow in these cases. However, earlier investigation reported that early stage turbulence was found in thermoacoustic flow conditions at critical Stokes Reynolds number as low as 70 [18]. It is therefore important to make sure that correct models are used in solving thermoacoustic flow

conditions. In this study a laminar model, a transition model and a turbulence model were solved for every cases and the differences between the results obtained from all the models are discussed with comparison to experimental data. Numerical model that provides velocity value that is closest to the value from experimental data will be selected as the model that best represents the fluid dynamics of the flow at the specific drive ratio of the thermoacoustic flow setup. The laminar model was solved using Navier-Stokes equation. The two-equation Shear-Stress-Transport (SST) $k-\omega$ model was proven to be the best model that can capture the fluid dynamics of flow within the viscous and inviscid regions of the thermoacoustic environment when turbulence is detected in the flow [18]. Hence, the turbulence models were solved using the Shear-Stress Transport (SST) two-equations $k-\omega$ model and the transition flow conditions were investigated via the Langtry-Menter four-equation Transition SST model. The models were solved using an unsteady pressure-based implicit solver with the application of the Pressure-Implicit with Splitting Operators (PISO) scheme for the pressure-velocity coupling.

A second-order discretization method was selected for discretization of time, as well as turbulent transport equations. The flow field was initialized using standard initialization method before calculations were made. The time step size used was $1/1200f$. The convergence was set at 10^{-6} for energy equation while the value of 10^{-3} was used for the continuity, momentum and turbulence transport equations. The 2D unsteady (transient) model is calculated using computers with processor Intel (R) Xeon (R) CPU E5-2609v3, equipped with 1.90GHz and an installed memory (RAM) of 8GB.

Figure 3 shows the examples of the time history of velocity for drive ratio of 3% taken at the middle location of the stack for the two flow frequencies. The dashed-box placed at the early stage of the cycles shows the evolution of cycles during the starting up of the process until the cycles reached a steady oscillatory flow condition. The vertical dashed-lines represent the duration of one flow cycle.

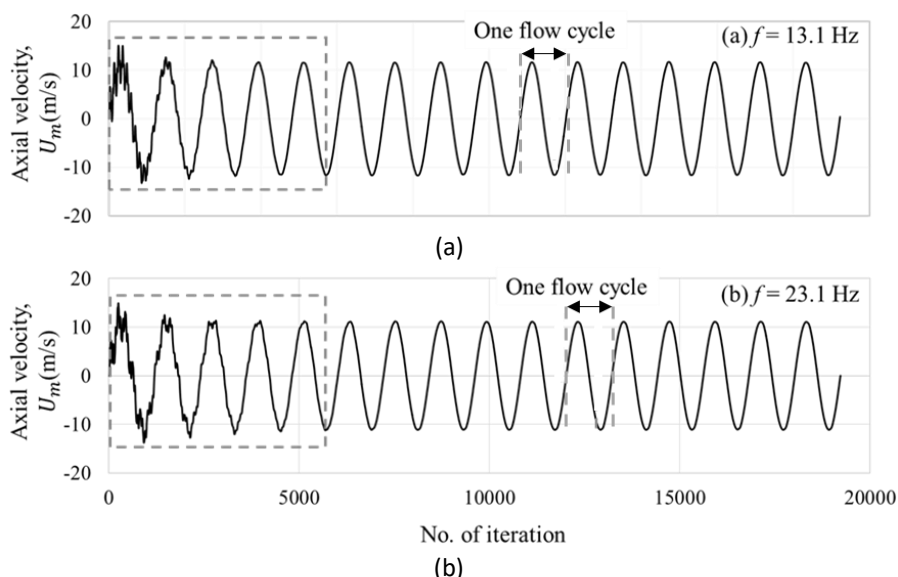


Fig. 3. The time history of the area-weighted average of axial velocity for flow frequencies of, (a) 13.1 Hz and (b) 23.1 Hz

The steady oscillatory flow condition is a condition where the flow oscillates in a steady manner (smooth sine wave) over time. At this moment onwards, pressure and velocity are constant throughout the flow cycle. This is a stage where flow is stabilized and analysis can be proceeded. In order to ensure that the steady oscillatory condition is met, the models were computationally solved for at least sixteen flow cycles. For the lower flow frequency of 13.1 Hz the total computational time to calculate the sixteen flow cycles for laminar model, Transition SST and SST $k-\omega$ turbulence models

are corresponding to 160.6, 311.5 and 305.9 hours, respectively. While for flow frequency of 23.1 Hz the total computational time for laminar model, Transition SST and SST k- ω turbulence models are 142.3, 326.4 and 246.7 hours, respectively. It was observed that at higher flow frequency, the computational model is solved at faster rate compared to lower flow frequency.

2.3 Experimental Setup for Model Validation Purposes

An experimental test rig of the standing wave thermoacoustic system was designed and fabricated at Universiti Teknikal Malaysia Melaka and the rig is as shown in Figure 4. It consists of a loudspeaker (700 W subwoofer - Model PD1860) as a driver and a resonator (made of mild steel) with a test section with size of 14 cm (width) x 14 cm (height). The test section roof and wall are made of acrylic. An aluminum parallel-plate structure was placed inside the test section area, and its geometrical properties such as plate thickness and plate gaps are kept constant. The resonator was designed with several segments so that the total length could be altered and two flow conditions with different resonance frequencies of 13.1 Hz and 23.1 Hz could be achieved. The designed was originally based on theoretical calculation using equations in the Linear Thermoacoustic Theory [5]. However, due to unforeseen factors such as the fabrication difficulties, the resonance frequency of the current rig is slightly over the original value as found in the theoretical calculation. As these differences lead to a small error in the flow amplitude ($\approx 1\%$) and results (i.e. velocity profile and vortex), it can be safely neglected. To measure the flow velocity for the validation purpose, a hot wire (Sentry model ST732, accuracy: $\pm 0.03 + 3\%$ m/s) is used. The probe was placed at a distance $4 * d$ (≈ 12 mm) from the end of the parallel-plate stack.

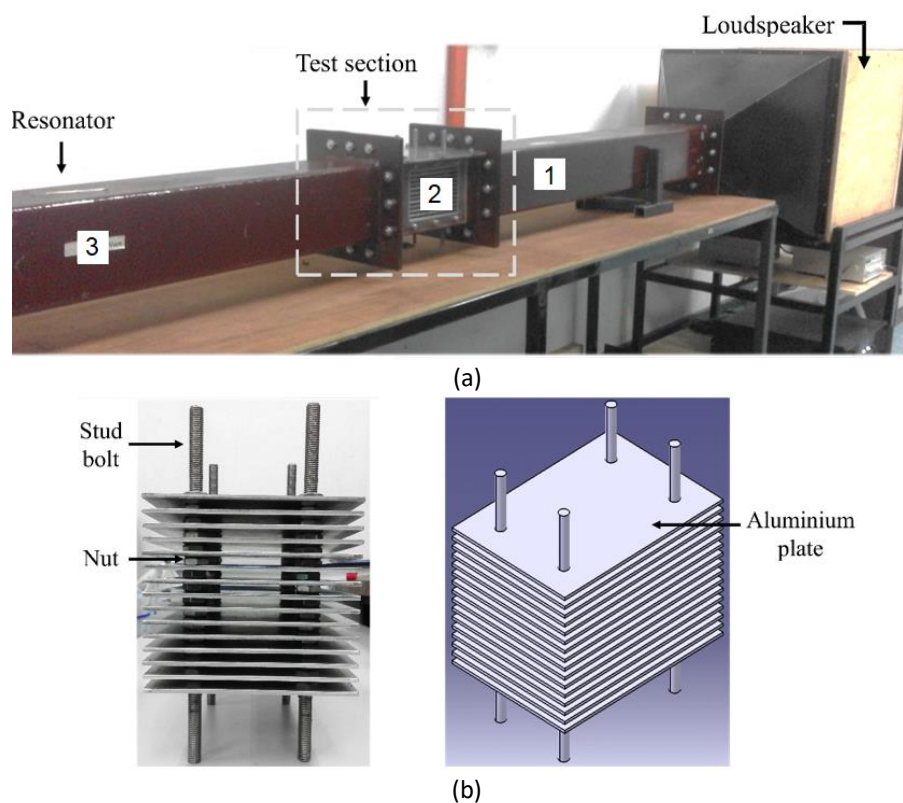


Fig. 4. (a) The test rig: (1) Upstream resonator (2) Test section and (3) downstream resonator (b) The front view (left) and the technical drawing (right) of the stack

3. Results

This section starts with the results of model validation. The validated models are then used to produce results of velocity profiles and vortex shedding patterns at two different flow frequencies. The results represent the fluid dynamics of oscillatory flow inside thermoacoustic environment with two different flow frequencies.

3.1 Model Validation and Verification

The numerical models were validated by comparing the results of velocity amplitude with the experimental data and theoretical calculations for range of drive ratio between 0.73% and 1.6%. The theoretical value of velocity was obtained by dividing the mass flux as defined in Eq. (4) with the density of the fluid. The results are as shown in Figure 5.

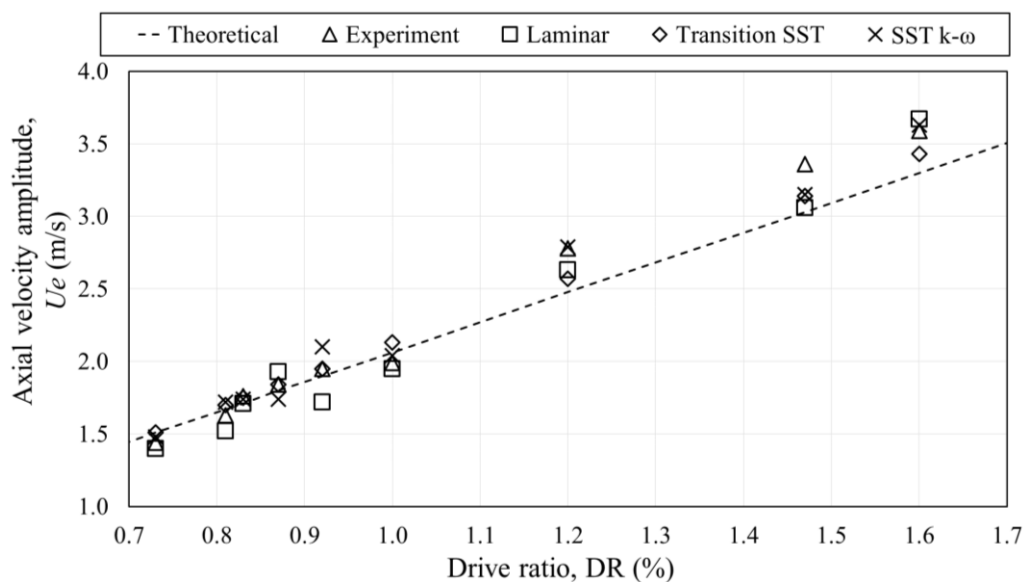


Fig. 5. Comparison between axial velocity amplitude from theoretical calculations, experimental results and numerical models for flow frequency of 13.1 Hz

Based on Figure 5, it is observed that the change of velocity with drive ratios from CFD models and experimental results are linear, following the line of theoretical values, especially for the results with drive ratios lower than 0.9%. At low drive ratio of 0.73%, the axial velocity amplitude value from laminar model was found to be the value that is closest to experimental result. However, as drive ratio increases, turbulence models are found to be the models that provide velocity values closest to experiments. It was found that the Transition SST turbulence model is the best model for the drive ratio of 0.81% and 1.0%. This indicates that flow at these drive ratios is transitional flow. For drive ratio of more than 1.2%, the SST k- ω turbulence model was found to provide values that are closest to the experimentally measured values. This shows that flow in this region exhibits a fully turbulence fluid dynamics behaviour. More importantly, it is also observed that the experimental values are deviating from the linear line of theoretical prediction as drive ratio increases. This indicates the presence of disturbances such as turbulence. The same observation was also reported by Mohd Saat and Jaworski [18] where deviation from the laminar prediction indicated the presence of an early stage turbulence in the flow. They reported that turbulence models provided the best velocity profiles and vortex shedding patterns that were similar to the experimental observations of PIV results. Turbulence changes the flow behaviour within the boundary layer leading to the special

feature of vortex shedding pattern at the end of the structure [18]. Hence, turbulence model seems to be able to capture the fluid dynamics correctly, through Reynolds stresses contribution in the models. Mohd Saat and Jaworski [18] also reported that the deviation of velocity data from the prediction of the one-dimensional linear thermoacoustic theory indicates that the influence of turbulence is stronger. Hence, by setting the observation reported by Mohd Saat and Jaworski, [18] as a benchmark, it is fair to conclude that the onset of turbulence could be estimated based on the observation of values that deviates from the predictions of laminar and/or linear models. The details of this observation method can be found in Mohd Saat and Jaworski [18]'s work, which is helpful for choosing suitable numerical model in solving fluid dynamics of the oscillatory flow for all the investigated drive ratio.

For the purpose of validation, the numerical models were solved for range of drive ratio as set in the experimental works. It is also worth mentioning here that the limitation of the experimental setup leads to difficulty to experimentally measure the velocity amplitude at very low and very high drive ratio. At low drive ratio, the low value of velocity could not be reliably detected by the sensor presumably due to the limitation of the sensor itself. For dynamic flow situation with low flow amplitude, a sensor with high sensitivity and high resolution is needed for accurate measurement. This leads to limited operating conditions. Choosing a sensor with wide range of operating condition commonly leads to lack of sensitivity and resolution. In this study, the dynamic flow amplitude oscillates at low range (approximately between 1 m/s to 5 m/s). At range lower than 1 m/s, the oscillation of flow was not easily detected by the available hotwire. The oscillating movement of the flow makes it harder to detect the flow amplitude. Hence, experimental measurements at lower range was omitted. On the other end, when the drive ratio is high, the experimental rig vibrates and therefore reliable values of velocity readings could not be obtained as well. It is worth mentioning here that every possible effort was done to ensure that data can be collected for wider range of flow amplitudes for the purpose of validation of numerical model. The rig was fitted to the table carefully with the addition of rubber seals at several joints to help reduce the vibration issues. Unfortunately, vibration becomes stronger as flow amplitude becomes bigger (i.e. higher drive ratio) and this limits the data that can be collected experimentally. Further investigation on the preventive methods for measurements at higher flow amplitudes should be carried out for future works. Nevertheless, the available experimental data (that was collected at conditions where vibration was not observed) are sufficient for the purpose of model validation. The similar trend of velocity increase between the numerical and experimental results indicate that the numerical models are correct.

Figure 6 shows the change of velocity amplitude with drive ratio for flow frequency of 23.1 Hz from experimental measurements, numerical modelling and theoretical calculation. In this case, with a higher flow frequency, it is observed that the numerical models produced results that are closer to the theoretical values. However, the experimental data are significantly deviated from the prediction of the linear theory with the largest difference of 14% as recorded at a drive ratio of 1.52%. Meanwhile, the numerical predictions are only slightly higher than the theoretical values and a smaller deviation is seen at the same drive ratio, which is about 2.17%. It is worth mentioning here that the deviation could be attributed to a noticeable vibration of the experimental rig when operating at a flow frequency of 23.1 Hz. This vibration could lead to an additional streaming inside the rig and this could bring an error to the measured value of velocity. Extending the experimental works with the current setup is not possible at this moment as the vibration becomes stronger when the drive ratio increases. Yet, the pattern of the increase of velocity with the increment of drive ratio is correctly predicted by the numerical models. The values obtained from the numerical works are within the range predicted by the theory and experiment. Hence, the models can still provide useful

insight about fluid dynamics of flow inside the system in an ideal situation where additional vibration is absent.

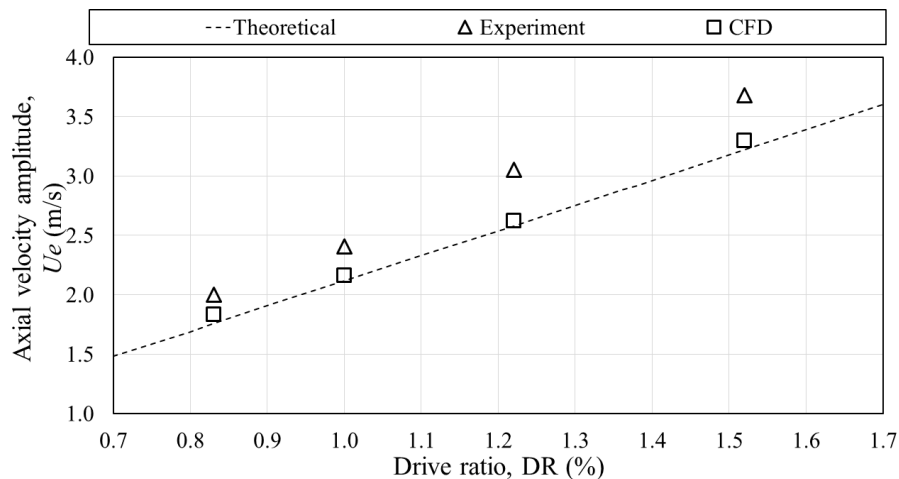


Fig. 6. Comparison between axial velocity amplitude from theoretical calculations, experimental results and numerical models for flow frequency of 23.1 Hz.

3.2 Velocity Profiles

The velocity profiles for both flow frequencies of 13.1 Hz and 23.1 Hz are as shown in Figure 7. The profiles represent the axial velocities from the plate surface (wall) up to middle of the plate spacing, $y = 3$ mm. Symmetrical results are expected from $y = 3$ mm to 6 mm to the top plate.

The results show that changes of velocity amplitude with drive ratio are the same for both flow frequencies. The slight difference in value is probably due to the effect of drastic flow movement as frequency increases. For both the flow frequency, maximum value of velocity appears not at the core but at a location near to the plate wall. For 13.1 Hz, the maximum point of velocity occurred at $y = 1.42$ mm while for flow frequency of 23.1 Hz, the maximum point of velocity is at 1.16 mm. This is the common feature of the oscillatory flow known as annular flow. It is also sometimes referred to as the ‘overshooting’ phenomenon.

As flow frequency increases, the maximum point of velocity tends to be closer to the wall due to the thinner viscous penetration depth. It is observed that, for both flow frequencies, the velocity profiles for all the three drive ratios of 0.45%, 0.65% and 0.83% can be safely modelled using laminar model. Modelling the flow using turbulence model will not give significant impact on the flow feature due to small influence of Reynolds stresses components. The increase of flow frequency leads to a rapid flow conditions where fluid flows faster with time but at the same amplitude of velocity. The rapidness of flow could lead to additional vibration to the system. It is commonly assumed that the rapid flow conditions lead to earlier start of turbulence. The current result indicates that turbulence is not present at low drive ratios even when the flow becomes rapid as frequency increases. However, as drive ratio increases (i.e. velocity amplitude increases) turbulence starts to show. This is as shown in Figure 8.

Figure 8 shows the velocity profiles for drive ratios of 2.0 % and 3.0 %. The maximum velocity amplitudes for these drive ratios, $U_{m,max} < 12$ m/s. This corresponds to a Reynolds number that is not exceeding 4800 (calculated based on the size of gap between the plates $D = 6$ mm). At these high drive ratios, the estimation of velocity profiles from the three models of laminar, transition SST and

the SST k- ω models are slightly different. The differences can be seen happening at two distinct regions denoted as dashed circles '1' and '2' in Figure 8. The deviation in these two regions are related to the change in turbulent kinetic energy (TKE) values in that regions. It is observed that the turbulent kinetic energy values increase as drive ratio increases. This can be seen by comparing results between Figure 8(a) and (b) for frequency of 13.1 Hz. The same observation can be seen when comparing Figure 8 (c) and (d) for higher flow frequency of 23.1 Hz. However, as frequency increases the turbulent kinetic energy decreases. This can be seen by comparing the profiles in Figure (b) and (d). The slightly odd turbulent behaviour of the case with drive ratio of 2.0% and a frequency of 23.1 Hz may be related to the small influence of turbulence within the thin boundary layer of the transition high flow frequency condition.

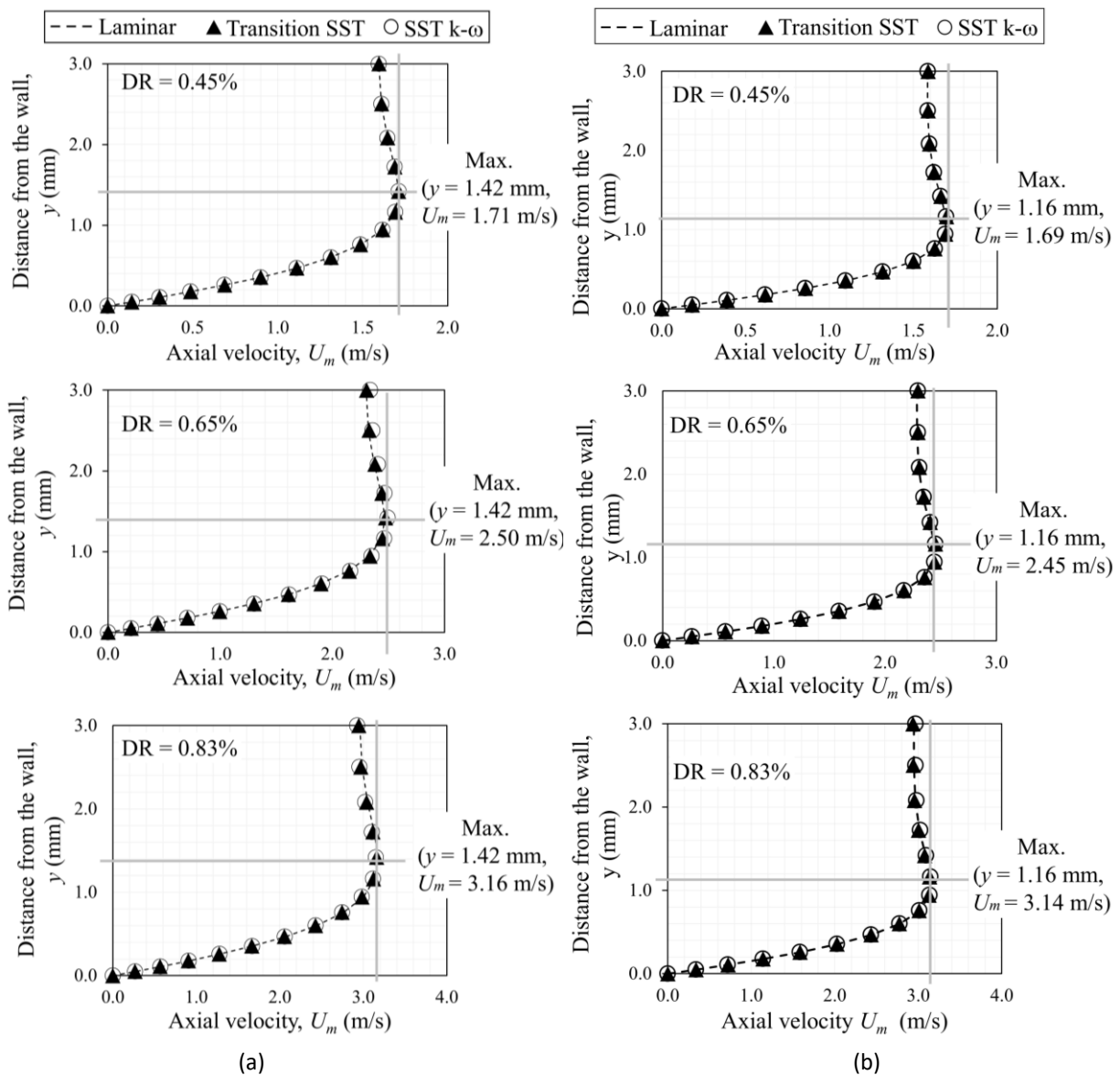


Fig. 7. Velocity profile at the maximum flow amplitude for drive ratios of DR = 0.45%, DR = 0.65% and DR = 0.83% and flow frequency of (a) 13.1 Hz and (b) 23.1 Hz

A higher flow frequency leads to a more rapid flow behaviour. Hence it was expected that turbulence should be more prominent. However, the reduction of turbulent kinetic energy as frequency increases, as reported in Figure 8, may be due to the fluid displacement. The fluid

displacement is shorter as flow frequency increases. This could lead to the small influence of turbulence on the mean flow.

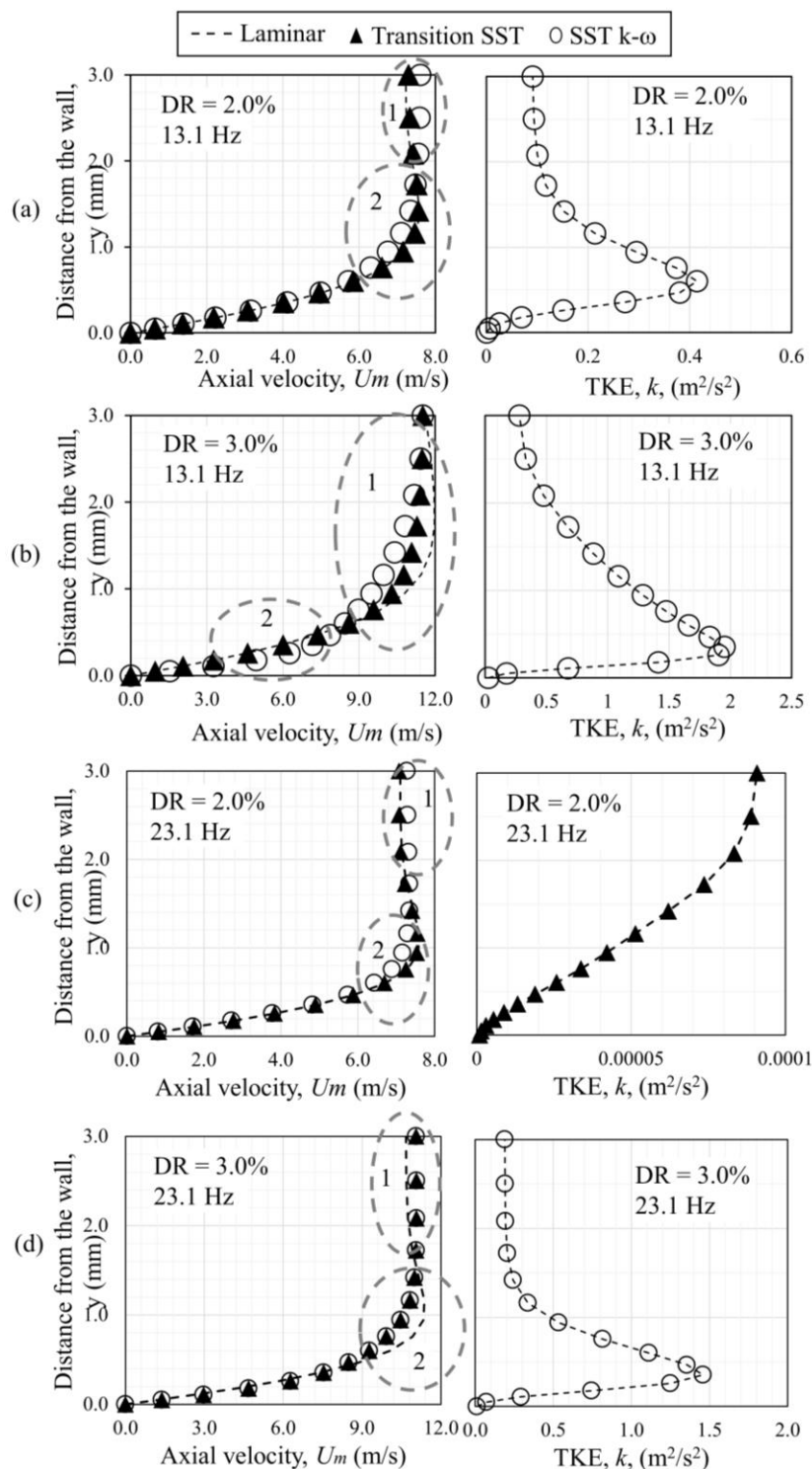


Fig. 8. Comparison of velocity profiles (left) and turbulent kinetic energy, TKE, (right) between drive ratios of 2.0 % and 3.0 % and flow frequencies of 13.1 Hz and 23.1 Hz

The velocity is related to fluid displacement through a relationship of $u = \omega\delta$, where u , ω and δ are the velocity amplitude, the angular velocity and the fluid displacement, respectively. Also, the

angular velocity, ω in this study are calculated using the selected flow frequency values ($\omega = 2\pi f$). The velocity amplitudes for different flow frequency but at the same drive ratio are approximately the same, as shown earlier in Figure 7. However, it is learned from the relationship between velocity amplitude and the fluid displacement that while velocity amplitude is the same, the fluid is displaced to a shorter distance as frequency increases.

3.3 Vortex Shedding

Figure 9 shows the vortex shedding pattern at the end of plate for several selected phases out of twenty phases of a flow cycle. For ease of analysis, the flow cycle was divided into twenty phases with the first ten phases representing the acceleration parts and the second ten phases is representing the deceleration stage. The phases ϕ_2, ϕ_5, ϕ_8 , as shown in Figure 9, are the selected few phases that are representing the acceleration stage while ϕ_{11} represents the stage when the flow starts decelerating. The results are shown for two different flow frequencies with DR = 0.83%. The left side of Figure 9 shows the vortex pattern for flow frequency of 13.1 Hz while the right side of the figure shows the vortex pattern for frequency of 23.1 Hz.

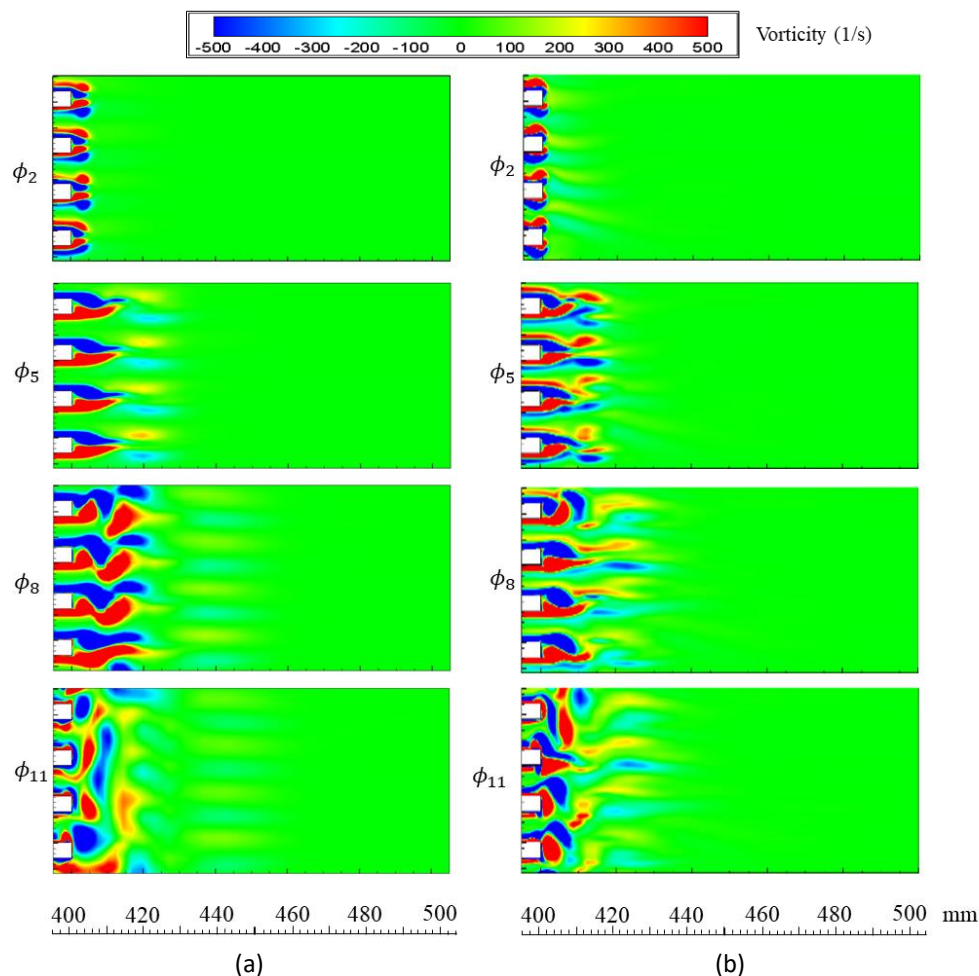


Fig. 9. The vortex shedding pattern of selected phases of flow for flow frequency of (a) 13.1 Hz and (b) 23.1 Hz

By comparing the vortex pattern between two different flow frequencies but at the same phase of a flow cycle, (i.e. comparing the left and right patterns for each phases of $\phi_2, \phi_5, \phi_8, \phi_{11}$), it can be

seen that as the frequency increases, the vortex sheds to a slightly shorter distance after the end of plate. For an example, the main vortex at ϕ_8 sheds to a distance of ≈ 20 mm after the end of the plate when the frequency is 13.1 Hz but at higher frequency of 23.1 Hz, the main vortex at the same phase, ϕ_8 sheds to a shorter distance of ≈ 12 mm. This distinguished pattern can be seen as early as phase ϕ_2 , where the cycle is just started. Interestingly, a break-up of elongated vortices is more significant for the high frequency during phase ϕ_5 , even though a formation of a pair of attached symmetric vortices at the end of the plate occurs only for the low frequency in the earlier phase (ϕ_2).

On the other hand, the presence of the secondary layer of vortex seems stronger for higher flow frequency compared to the lower flow frequency. This indicates the presence of additional streaming in the flow. Phase ϕ_{11} shows the beginning of suction stage, where the vortex starts reversing as the flow reverses back into the channel, obviously seen with the lower frequency. The reversing vortex tends to interfere with the flow inside the channel hence resulting to the annular effect of velocity profile as seen earlier in Figures 7 and 8. Regardless of flow frequency, the vortex streets are still remaining at the end of the plate during phase ϕ_{11} .

4. Conclusions

Fluid dynamics of an oscillatory flow at two different flow frequencies are reported based on results obtained from an experimentally validated numerical models. Experimental works provided velocity amplitude data for the purpose of model validation. Good match was found for flow frequency of 13.1 Hz while similar pattern of velocity change with the change of drive ratio was observed for flow with high frequency of 23.1 Hz. Numerical models also show that the start of turbulence is delayed as the frequency increases. This is based on the velocity profiles plotted within the channel of the parallel-plate structure. The delay of the start of turbulence within the channel may be due to the shorter travel distance of air as frequency increases. Hence, the vorticity at the end of plates will not penetrate too far into the channel as the flow reverses. As a result, flow tend to remain laminar particularly at the centre of the channel. While the current validated models are sufficient for early prediction of flow morphology inside thermoacoustics, improvements are still needed to be done in both the numerical works as well as experimental works in order to obtain perfect match that could explain the physics of flow. This includes the streaming of flow that is related to higher order vibration particularly for high flow frequency. The use of vibration silencer such as those reported in [22] may be considered in future research work provided that it's use is not interfering with the "thermoacoustic effect" that is needed for the system. More numerical as well as experimental works are needed to verify the complicated flow topology of oscillatory flow inside thermoacoustic environment so that a better and a well-established foundation for fluid dynamics of an oscillatory flow could be developed for thermoacoustic system.

Acknowledgement

This research work was conducted using facilities at the Universiti Teknikal Malaysia Melaka and is supported by a short term grant: PJP/2019/FKM (7A)/S01679.

References

- [1] Khattak M. A., Yahya T. M. H. T., Sallehudin M. W. M., Ghazali M. I. M., Abdullah N. A. "Global Energy Security and Eastern Europe: A Review." *Journal of Advanced Research Design* 45, no. 1 (2018): 19-42
- [2] Sidik N. A. C., Alawi O. A. "Computational Investigations on Heat Transfer Enhancements Using Nanorefrigerants." *Journal of Advanced Research Design* 1, no. 1 (2014): 35-41

- [3] Mustaffa S. H. A., Mohd Saat F. A. Z., and Mattokit E. "Turbulent Vortex Shedding across Internal Structure in Thermoacoustic Oscillatory Flow." *Journal of Advanced Research in Fluid Mechanics and Thermal Sciences* 46, no. 1 (2018): 175-184.
- [4] Kazuto Kuzuu and Shinya Hasegawa. "Effect of non-linear behaviour on heat transfer in a thermoacoustic engine core." *International Journal of Heat and Mass Transfer* 108 (2017): 1591-1601.
- [5] Swift, G. W. *Thermoacoustics: A Unifying Perspective For Some Engines And Refrigerators*. S.L.: Springer International PU, 2018
- [6] Nouh M., Aldraihem O., and Baz A. "Piezo-driven thermoacoustic refrigerators with dynamic magnifiers." *Applied Acoustics* 83 (2014): 86-99.
- [7] Sharify E. M., and Hasegawa S. "Traveling-wave thermoacoustic refrigerator driven by a multistage traveling-wave thermoacoustic engine." *Applied Thermal Engineering* 113 (2017): 791-795.
- [8] Qiu L. M., Lai B. H., Li Y. F., and Sun D. M. "Numerical simulation of the onset characteristics in a standing wave thermoacoustic engine based on thermodynamic analysis." *International Journal of Heat and Mass Transfer* 55, no. 7-8 (2012): 2200-2203.
- [9] Bi T., Wu Z., Zhang L., Yu G., Luo E., and Dai W. "Development of a 5 kW traveling-wave thermoacoustic electric generator." *Applied energy* 185 (2017): 1355-1361.
- [10] Agarwal H., Vishnu R. Unni, K. T. Akhil, N. T. Ravi, S. Md Iqbal, R. I. Sujith, and Bala Pesala. "Compact standing wave thermoacoustic generator for power conversion applications." *Applied Acoustics* 110 (2016): 110-118.
- [11] Shen Chao, Hong-Xin Li, Dong-Wei Zhang, Peng Yu, Na Pan, and Shuang-Feng Wang. "Study on the heat transfer characteristic of solar powered thermoacoustic prime mover at different tilted angles." *Applied Thermal Engineering* 103 (2016): 1126-1134.
- [12] Abdoulla-Latiwish Kalid OA, and Artur J. Jaworski. "Two-stage travelling-wave thermoacoustic electricity generator for rural areas of developing countries." *Applied Acoustics* 151 (2019): 87-98.
- [13] Yahya, Samir Gh, Xiaoan Mao, and Artur J. Jaworski. "Experimental investigation of thermal performance of random stack materials for use in standing wave thermoacoustic refrigerators." *International Journal of Refrigeration* 75 (2017): 52-63.
- [14] Jin, T., Yang R., Wang Y., Feng Y., and Tang K. "Acoustic field characteristics and performance analysis of a looped travelling-wave thermoacoustic refrigerator." *Energy Conversion and Management* 123 (2016): 243-251.
- [15] Alcock A. C., Tartibu L. K., and Jen T. C. "Experimental investigation of an adjustable thermoacoustically-driven thermoacoustic refrigerator." *International Journal of Refrigeration* 94 (2018): 71-86.
- [16] Zolpakar N. A., Mohd-Ghazali N., and Mawahib Hassan El-Fawal. "Performance analysis of the standing wave thermoacoustic refrigerator: A review." *Renewable and sustainable energy reviews* 54 (2016): 626-634.
- [17] Abdoulla-Latiwish Kalid OA, Xiaoan Mao, and Artur J. Jaworski. "Thermoacoustic micro-electricity generator for rural dwellings in developing countries driven by waste heat from cooking activities." *Energy* 134 (2017): 1107-1120.
- [18] Mohd Saat F.A.Z., and Jaworski A.J. "Numerical predictions of early stage turbulence in oscillatory flow across parallel-plate heat exchangers of a thermoacoustic system." *Applied Sciences* 7, no. 7 (2017): 673.
- [19] Mao Xiaoan, and Artur J. Jaworski. "Application of particle image velocimetry measurement techniques to study turbulence characteristics of oscillatory flows around parallel-plate structures in thermoacoustic devices." *Measurement Science and Technology* 21, no. 3 (2010): 035403.
- [20] Mohd-Ghazali N., and Liew Kim Fa. "Numerical Simulation Of Flow Surrounding A Thermoacoustic Stack: Single-Stack Against Double-Stack Plate Domain." *Jurnal Teknologi* 78, no. 8-4 (2016): 119-125.
- [21] Feldmann D., and Wagner C. "On the influence of computational domain length on turbulence in oscillatory pipe flow." *International Journal of Heat and Fluid Flow* 61 (2016): 229-244.
- [22] Ismail A. Y., Chen M. F., Azizi M. F., Sis M. A. "Experimental Investigation on the use of Natural Waste Fibres as Acoustic Material of Noise Silencer." *Journal of Advanced Research in Materials Science* 22, no. 1 (2016): 1-10.